Detection, localization and characterization of damage in plates with an *in situ* array of spatially distributed ultrasonic sensors

View the article online for updates and enhancements.

Detection, localization and characterization of damage in plates with an *in situ* array of spatially distributed ultrasonic sensors

Jennifer E Michaels

School of Electrical and Computer Engineering, Georgia Institute of Technology, Atlanta,
GA 30332-0250, USA

E-mail: jennifer.michaels@ece.gatech.edu

Abstract

Permanently attached piezoelectric sensors arranged in a spatially distributed array are under consideration for structural health monitoring systems incorporating active ultrasonic methods. Most damage detection and localization methods that have been proposed are based upon comparing monitored signals to baselines recorded from the structure prior to initiation of damage. To be effective, this comparison process must take into account any conditions other than damage that have changed the ultrasonic signals. Proposed here is a two-step process whereby damage is first detected and is then localized and characterized. The detection strategy considers the long time behavior of the signals in the diffuse-like regime where distinct echoes can no longer be identified. The localization strategy is to generate images of damage based upon the early time regime when discrete echoes from boundary reflections and scattering sites are meaningful. Results are shown for an aluminum plate with artificial damage introduced in combination with temperature variations. The loss of local temporal coherence combined with an optimal baseline selection procedure is shown to be effective for the detection of damage, and a delay-and-sum imaging method applied to the residual signals both localizes the damage and provides characterization information.

(Some figures in this article are in colour only in the electronic version)

1. Introduction

A spatially distributed array of permanently mounted piezoelectric sensors is one possible configuration for an active ultrasonics approach to structural health monitoring. These sensors, when bonded to plate-like structures such as are common in the aerospace industry, readily generate Lamb waves which propagate relatively long distances while maintaining good sensitivity to damage [1]. With such an array, each sensor can act in turn as a transmitter and the remainder as receivers, with signals from all transducer pairs being recorded. The advantage of this arrangement is that any potential flaw location is interrogated from a variety of angles, maximizing the probability that it can be detected. If the structure is geometrically simple, discrete damage appears as the presence of an additional echo scattered or reflected from the damage site, as is common for guided wave-based nondestructive testing methods [2]. For a structure of realistic geometrical complexity, this approach to damage detection breaks down because the recorded signals become too complex for specific echoes to be readily identified, especially small echoes typical of those scattered from damage [3].

A number of methods have been proposed for detecting damage based upon comparing signals to baselines recorded from the undamaged structure. The simplest method is to subtract two signals and compute either the peak amplitude or the energy of the residual [4]. This approach is very effective if damage is the only factor causing the signals to change. Additional time and frequency domain features based upon the comparison of two signals have also been proposed for damage

detection. Gao *et al* [5] calculate a signal difference coefficient as $1 - \rho$, where ρ is the correlation coefficient between the two signals being compared. This coefficient is not dependent upon overall amplitude changes such as would affect simple waveform differencing, but is only dependent upon signal shape changes. Mal *et al* [6, 7] compute a damage index based upon the spectra of the two signals being compared; this index also does not depend upon overall amplitude changes. Michaels *et al* [8] consider a set of time and frequency domain differential features and evaluate various combinations for damage detection. Lu and Michaels [9] also consider a differential feature approach, and apply data fusion methods to improve the probability of detection while maintaining a low false alarm rate.

The idea of baseline comparison also serves as the foundation for various algorithms that have been proposed for localizing damage. In the ideal case, if the two signals being compared are subtracted, the first arrival of the residual signal will be the scattered echo from the flaw. If the propagation mode and corresponding group velocity are known, then the total path length from transmitter to flaw to receiver can be calculated. This path can then be used to construct an ellipse with the two transducer locations as foci, and the flaw is constrained to fall on this ellipse. Lemistre and Balageas [10] compute a set of localization points by solving the ellipse intersection equations two at a time. Tua *et al* [11] successfully locate notches of various orientations by constructing multiple ellipses from various transducer pair combinations and visually determining where they intersect. Michaels *et al* [12] similarly construct ellipses, but localize damage via the sum of the distances to all of the ellipses calculated over the area of interest.

Other methods for localizing damage with spatially distributed arrays have been considered. The simplest approach, which is most effective for smaller transducer spacings, is to localize damage in the neighborhood of individual sensors. This is the approach taken by Mal *et al* [6, 7] by plotting damage indices as a function of transducer locations. The RAPID (reconstruction algorithm for probabilistic inspection of defects) method introduced by Zhao *et al* [13] expands upon this idea by spatially distributing and summing signal difference coefficients in elliptical patterns for all transducer pairs. Another class of localization methods is the 'delay-and-sum' type of algorithm such as is used for synthetic aperture and phased array imaging methods. Received signals are delayed and summed according to the appropriate spatial rule for each point on the image. Wang *et al* [14] used the concept of time reversal to motivate the delay calculations and then applied this method to the scattered (residual) signals to localize a glued mass on an aluminum plate. Michaels and Michaels [15, 16] have applied this method to both raw and envelope-detected residual signals to generate localization images of artificial damage in aluminum plates. They have also generated images at multiple frequencies and incorporated image fusion methods to obtain improved damage localization [17]. Fromme [18] has applied a delay-and-sum imaging method to both finite element and experimental data to locate defects in a steel plate with a stiffener.

Before any detection or localization method can truly be deemed effective, the two fundamental issues of structural complexity and environmental variations must be addressed. One approach to handling structural complexity is to specifically record a long time window which includes many reverberations within the structure, and employ algorithms such as coherence [19] and time reversal [20] methods which effectively utilize information in this time regime. The problem of a varying environment is more problematical, particularly for complex structures where the Green's functions are quite sensitive to changes in parameters such as temperature [21]. One approach is to independently measure the temperature and use this information to adjust the detection algorithm [22, 23]. Another approach is to record baselines at various temperatures and select the baseline data which are the best match to the current signals of interest [21, 24]. Regardless of the specific method employed, differential damage localization algorithms either implicitly or explicitly assume that the baselines are well matched to the current signals being processed.

Here we consider a two-stage strategy of damage detection followed by localization and characterization that is suitable for complex plate-like structures in a variable temperature environment. Damage detection is based upon the long time behavior of reverberating signals, and damage localization utilizes changes in the early time regime of the same signals. The damage localization stage also provides characterization information. Integral to the overall strategy is recording of a set of baseline signals spanning the temperature range of interest.

In section 2, the experimental procedures and recorded data are described. The strategy for damage detection is explained in section 3, and that of damage localization in section 4. Results are presented and discussed in section 5, and concluding remarks are made in section 6.

2. Experimental details

An aluminum plate (alloy 6061) of dimensions 610 mm $\times$ 610 mm $\times$ 4.76 mm was instrumented with a spatially distributed array of six piezoelectric transducers, as shown in figure 1. The transducers were fabricated in the QUEST (Quantitative Ultrasonic Evaluation, Sensing and Testing) Laboratory at Georgia Tech from 12.5 mm diameter, 2.25 MHz, compressional mode PZT discs. The discs were enclosed in a brass housing, backed with epoxy for protection, and bonded to the plate using a conductive epoxy. Transducers were excited using a commercial spike mode pulser receiver and a broadband front end multiplexer, with all 15 transmit–receive pairs being interrogated in turn. Signals were digitized at a sampling frequency of 25 MHz and with a resolution of 12 bits. A total of 50 waveforms were averaged for each signal acquisition to minimize the electronic noise.

Most of the energy coupled into the plate was in the frequency range below 1 MHz where the Lamb wave modes are excited by the transducers. The dominant mode is the S_0 mode, which is associated with a strong peak at approximately 250 kHz, but there is clear evidence of additional modes and frequencies. The cutoff frequency for the A_1 mode is approximately 330 MHz, and there was significant energy in
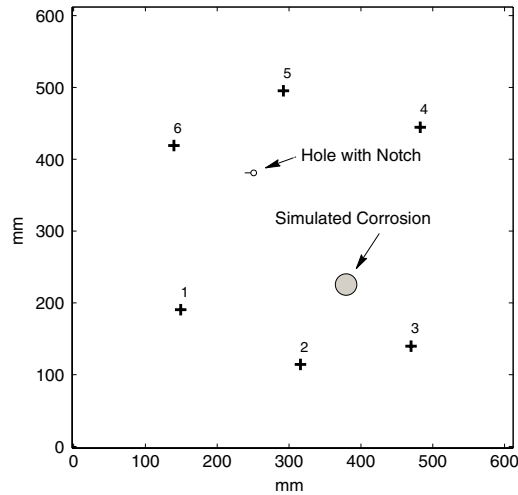
Figure 1. Diagram of the 6061 aluminum plate, where the $+$ symbols indicate transducer locations, the larger shaded circle is the region of simulated corrosion, and the small circle and line represent a drilled hole with a notch.

Table 1. Summary of data sets.

Data set (s)	Description	Temperature (°C)
1–60	Prior to drilling of hole	Variable, 17–37
61	Prior to drilling of hole	23.5
62	Drilled hole, 1.5 mm in diameter	23.5
63	Drilled hole, 2.0 mm in diameter	23.5
64	Drilled hole, 3.0 mm in diameter	23.5
65	Drilled hole, 4.0 mm in diameter	23.5
66	Drilled hole, 5.0 mm in diameter	23.5
67	Drilled hole, 6.0 mm in diameter	23.5
68–149	After drilling of hole	Variable, 18–34
150	After drilling of hole	23.7
151, 152, 153	Notch, 3.2 mm in length	24.2, 24.0 23.6
154, 155, 156	Notch, 6.4 mm in length	24.0, 23.8, 23.8
157, 158, 159	Notch, 9.5 mm in length	24.0
160–186	After machining notch	Variable, 18–34

the frequency domain well above this frequency. Considering the A_0 and S_0 modes, the expected range of group velocities is about 3 to 5.5 mm μs^{-1}, which corresponds to plate transit times ranging from about 100 to 200 μs. To ensure that many reverberations within the plate were recorded, the total time window for data acquisition was 4000 μs.

The starting structural condition of the plate was not undamaged, as a previous experiment had involved the creation of simulated corrosion by removal of about 1.2 mm of the thickness over a circular area about 30 mm in diameter. The center of this area was located at (379, 225 mm) relative to the lower left corner, and is indicated in figure 1 by the shaded circle. This condition of the plate is considered to be the baseline condition for the remaining experiments. Subsequent damage was introduced in two stages. The first was a 6 mm diameter hole, which was drilled in six steps at a location of (251, 381 mm). The second was a notch of length 9.5 mm originating from the left side of the hole to simulate a crack; the notch was machined in three length steps of 3.2, 6.4 and 9.5 mm. The hole and notch are also shown in figure 1.

Temperature changes were introduced to represent non-ideal operating conditions, and the plate was alternately cooled and heated before the hole was drilled, in between drilling the hole and machining the notch, and after the notch was machined. The range of temperatures considered was approximately 17–37 °C; temperatures were manually recorded using a Fluke 16 multi-meter with an integral temperature probe for some of the acquired waveforms, but were unrecorded for additional unattended measurements. A total of 186 data sets were recorded over a period of about 100 h, as summarized in table 1. The plate with both the simulated corrosion and the drilled hole was considered to be the baseline state for the notch experiment.

3. Damage detection

The strategy for damage detection is to compare the current signal with one or more baseline signals recorded from

the undamaged structure by calculating differential features that quantify how the signal has changed compared to the baseline. The term 'differential feature' describes a feature that compares two signals and is identically zero if the signals are the same. Note that the terms 'damage index' and 'signal difference coefficient' refer to specific differential features. If the only variable is damage, then many such differential features are effective for its detection. If in addition to damage there are also benign changes such as electronic noise and environmental variations, then these changes may significantly affect the ultrasonic signals and can easily overwhelm the often small signal changes caused by damage. The goal of the damage detection step is to utilize differential features which have both sensitivity to damage and selectivity in distinguishing damage from benign signal variations.

3.1. Differential features for quantifying signal changes

Considered here are three differential features which in some sense quantify the difference between a signal, $y(t)$, and a baseline, $x(t)$. The first differential feature, E_1, is the normalized squared error between the signal and baseline,

$$E_1 = \frac{\int_0^T [y(t) - x(t)]^2 \, dt}{\int_0^T x(t)^2 \, dt}. \tag{1}$$

Here T is the time window over which the signals are compared, and the error is normalized by the energy of the baseline signal. This and subsequent expressions are given in continuous time for clarity.

The second differential feature, E_2, is the drop in the correlation coefficient between the signal and baseline,

$$E_2 = 1 - \frac{\int_0^T [x(t) - \mu_x][y(t) - \mu_y] \, dt}{\sigma_x \sigma_y}. \tag{2}$$

This feature is the 'signal difference coefficient' of the RAPID algorithm proposed by Zhao et al [13]. The motivation behind this feature is that the correlation coefficient is affected only by changes in the shapes of the signals, not by amplitude variations as is the case for E_1.

The third differential feature, E_3, is the loss of local temporal coherence between the signal and baseline [19]. The
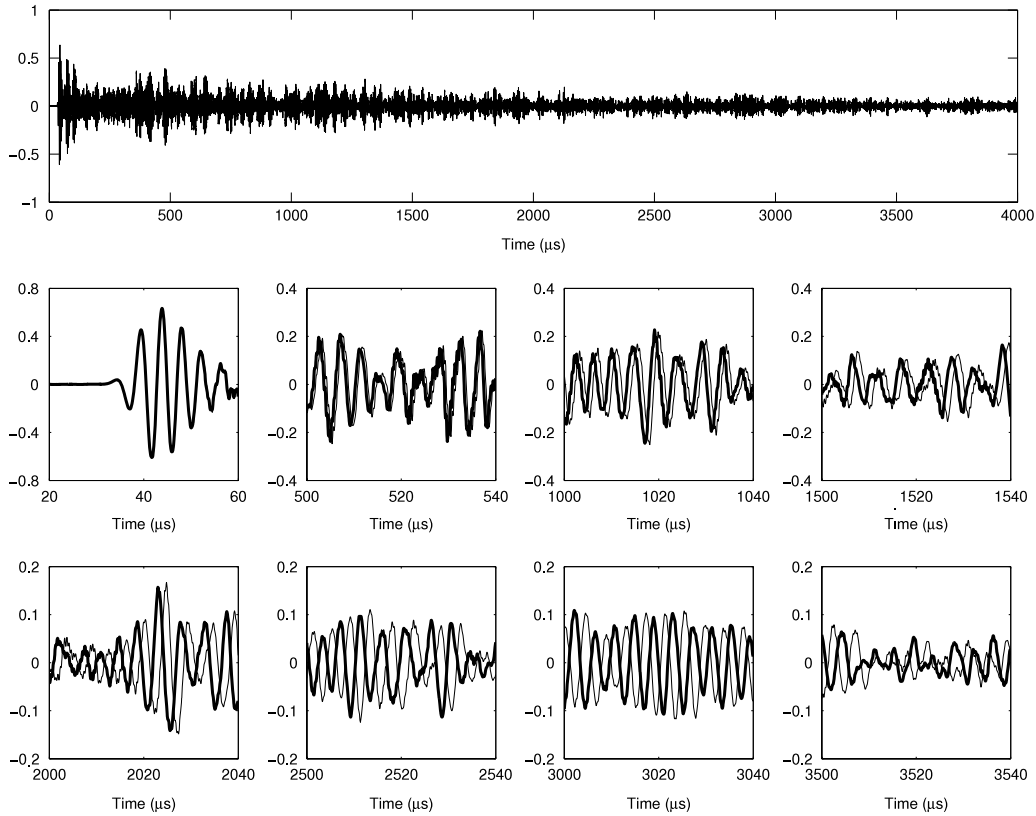
Figure 2. Signals recorded using transducers #1 and #2 prior to introduction of the hole and notch. The top plot shows the signal recorded at a measured temperature of 21.4 °C. The lower eight plots show zoomed regions of this signal (thick lines) along with the corresponding regions of a signal recorded at a measured temperature of 24 °C (thin lines), illustrating the time-dependent time shift caused by temperature changes.
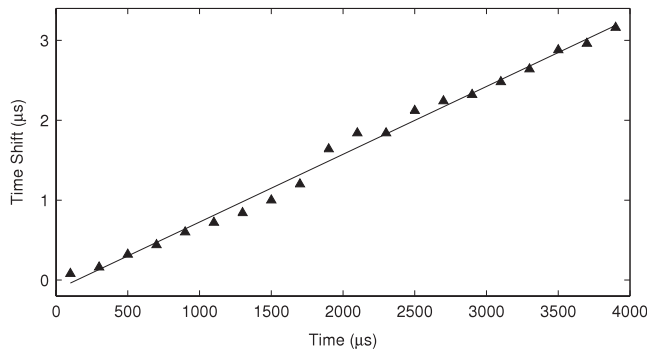
Figure 3. Time shift versus transit time computed from the signals of figure 2 for a measured temperature change of 2.6 °C. The time shifts were calculated from the short time cross correlation using sliding but non-overlapping windows of width 200 μs.

local temporal coherence between two signals is based upon the local (short time) cross correlation using a window of width ΔT which slides along both of the signals. The short time cross correlation between the two signals is

$$R_{xy}(\tau, t) = \frac{1}{\Delta T} \int_{t-\frac{\Delta T}{2}}^{t+\frac{\Delta T}{2}} x(s)w(s-t)y(s+\tau)w(s+\tau-t)\,\mathrm{d}s, \tag{3}$$

where $w(t)$ is a windowing function, typically rectangular, and τ is the cross correlation lag time. The short time cross correlation is normalized to obtain the local temporal

coherence,

$$\gamma_{xy}(\tau, t) = \frac{R_{xy}(\tau, t)}{\sqrt{R_{xx}(0, t)R_{yy}(0, t)}}. \tag{4}$$

Similar to the correlation coefficient, if two signals are identical in shape, the peak value of the local temporal coherence at every time t is unity even if the signal amplitudes are different. Unlike the correlation coefficient, the peak of the absolute value of the local temporal coherence is a function of time, and is a measure of how the shapes of two signals are changing with time, irrespective of amplitude differences and small time delays. The loss of local coherence, E_3, is how far the average local coherence drops below unity,

$$E_3 = 1 - \frac{1}{T} \int_0^T \max_\tau |\gamma_{xy}(\tau, t)| \, \mathrm{d}t, \tag{5}$$

where T is the time window for comparison. This single parameter is a measure of the overall difference in shape between the two signals. More information on the local temporal coherence method is given in [19].

3.2. Effect of temperature variations

The most common and unavoidable environmental change is temperature, which affects ultrasonic wave propagation by both changing the structural dimensions via thermal expansion and changing the longitudinal and shear bulk wave speeds.
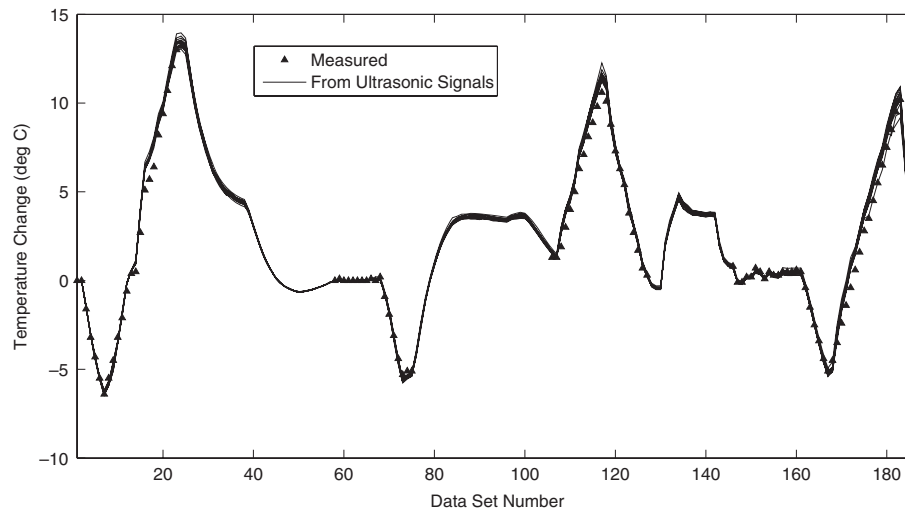
Figure 4. Temperature change relative to the first signal recorded as determined by measurement with a thermocouple (discrete data points) and by calculation from the short time cross correlation of the ultrasonic signals with the baseline signals of data set #1 (solid line for each transducer pair).

For a single ultrasonic echo, the result is a simple shift in time which is proportional to the distance traveled. If there are multiple echoes resulting from multiple wave modes and reflections, then the situation is more complicated. In the extreme, for completely diffuse waves, the first-order effect is a stretching or contracting of the time axis, and the second-order effect is shape distortion that increases with both transit time and the temperature difference [24, 25]. Most structures of interest support multiple guided wave modes, and each mode, in theory, will have a unique constant of proportionality relating the time shift to the propagation distance and thus the transit time.

Figure 2 illustrates the effect of temperature on a typical received signal from the plate of figure 1. The top plot shows a signal from transducers #1 and #2 recorded prior to damage at a measured temperature of 21.4 °C. The eight additional plots show zoomed regions of that signal at various times beginning with the first arrival. Shown on the same plots but with thinner lines are the corresponding regions of a signal from the same transducers but at a higher temperature (about 24 °C). The time-dependent time shift is clearly evident, ranging from virtually no shift of the first arrival to significant delays at longer times; the increased distortion with temperature is also visible.

The local time shift can be determined using the short time cross correlation, where the cross correlation of corresponding short time windows of the two signals is computed and the local time shift is the lag time of the local peak. Figure 3 illustrates the result of this process for the two signals of figure 2. Note that although there are some variations, the time shift versus transit time curve is essentially linear, as expected from diffuse wave theory, and the slope of the line is proportional to the change in temperature [24]. Thus, the difference in the temperatures at which two signals were recorded can be readily determined, even for plate-like structures for which the wave field is unlikely to be truly diffuse.

The coefficient relating the slope of the time shift versus transit time curve to temperature was determined from data sets #7 and #24, which were recorded at 17.1 °C and 36.7 °C, respectively; its value was calculated to be 0.000 281 64 °C^{-1}. Figure 4 shows the result of using this coefficient to calculate the relative temperature at which all 186 signals were recorded; signal #1, recorded at a temperature of 23.5 °C, is the reference. The discrete data points are the measured temperatures, which were recorded for only some of the signals, and are in excellent agreement with the temperatures calculated from the ultrasonic measurements. Differences most likely result from the estimated ±1 °C accuracy of the Fluke meter combined with the fact that all 15 signals were not recorded at exactly the same temperature because of the small time delay between measurements.

3.3. Optimal baseline selection

Integral to the damage detection strategy is the selection of the appropriate baseline data set for comparison to the current data set of interest. The simplest strategy is to use a single baseline data set recorded from the undamaged structure. This strategy is likely to fail because of the unavoidable temperature changes which strongly affect the signals. Another strategy is to select the optimal baseline from a set of signals recorded under a variety of conditions [21, 24]; if the conditions are temperature variations, then the goal would be to select the baseline signal recorded at the same temperature as the signal of interest. Determining the temperature from the short time cross correlation as discussed in section 3.2 is certainly a viable strategy for selecting the baseline, but is computationally expensive. Prior work has shown that finding the baseline signal with the minimum squared error achieves the same or better result but is computationally much less intensive [24]. That is the strategy employed here, with the selected baseline referred to as the optimal baseline.
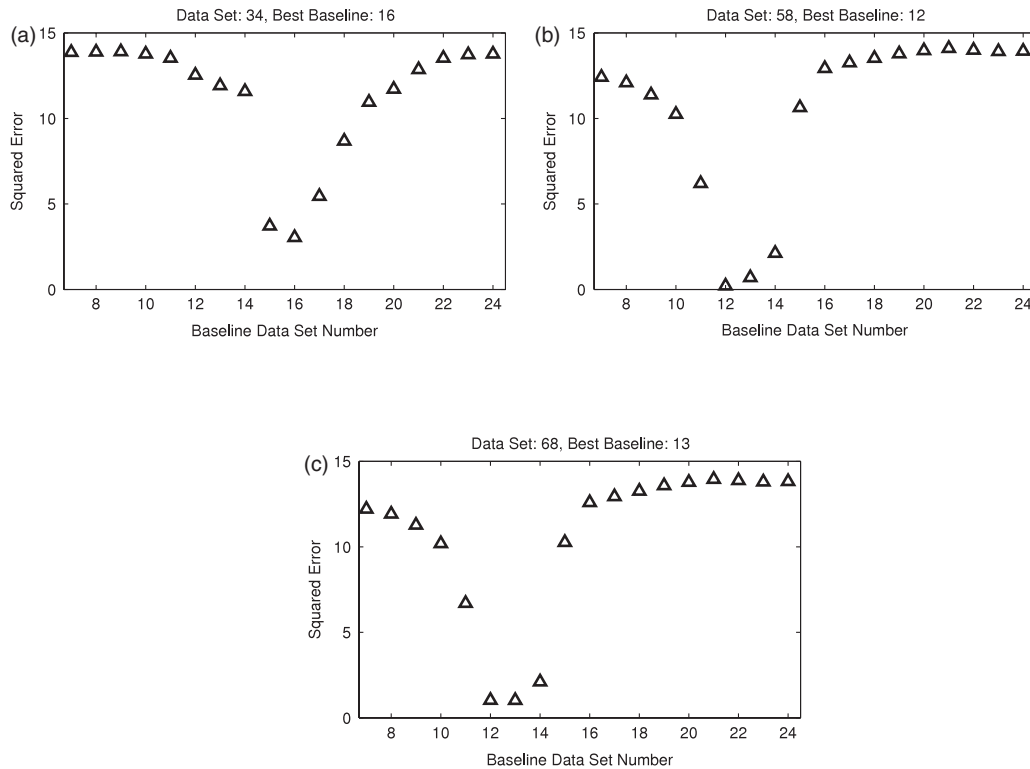
Figure 5. Total squared error for all 15 signals versus baseline data set number. (a) Data set #16 recorded at an unknown temperature, (b) data set #58 recorded at 23.5 °C prior to drilling of the hole, and (c) data set #68 recorded at 23.7 °C after the hole was drilled.

Figure 5 illustrates the optimal baseline selection process where the baselines consist of data sets #7 through #24, corresponding to temperatures ranging from 17.1 to 36.7 °C. Results are shown for three data sets, and the sum of the squared error over all 15 signals is plotted versus the baseline data set number. Note that the baselines and the first two data sets were recorded prior to damage, and the third data set was recorded after the introduction of damage. For figure 5(a), the temperature is unknown, and the best baseline is data set #16, recorded at 28.6 °C. For figure 5(b), the data set was recorded at a measured temperature of 23.5 °C, and the best baseline was found to be data set #12, recorded at 22.9 °C. Figure 5(c) is for a data set recorded at 23.7 °C after the hole was drilled, and the best baseline was found to be data set #13, recorded at 23.9 °C. The temperatures of the baseline and signal of interest yielding the best signal match do not always correspond to the minimum measured temperature difference. This discrepancy, as explained previously, is probably caused by a combination of meter inaccuracy and the fact that the signals from all 15 transducer pairs were recorded over a finite time interval during which the temperature may have slightly changed.

Note that the minimum error of figure 5(a) is greater than that of both figures 5(b) and (c), which indicates that the temperature match is not as close. The temperature difference between the signals of interest and the best baselines was ultrasonically determined to be 1.28 °C for figure 5(a) as compared to +0.17 and −0.47 °C for figures 5(b) and (c), respectively, which is consistent with the minimum errors shown in the plots. It is also important to note that the results of figure 5(c) correspond to a data set recorded after damage

was introduced. As was previously reported in [24], the experimental results indicate that determining the best baseline by this method is effective even in the presence of damage.

4. Damage localization

As discussed in section 1, several methods have been used to localize the damage in plate-like structures based upon changes in signals recorded from a spatially distributed array. The first method, which relies upon the intersection of ellipses, requires nearly perfect matching between the signal and the baseline so that arrival times from scattered signals can be determined. The second method, which spatially distributes and accumulates a differential feature in an elliptical pattern, implicitly assumes that the signals and baselines are well matched. Here we utilize the third method, a delay-and-sum algorithm where residual signals from the various transducer pairs are shifted and averaged to construct an image of the damage.

4.1. Signal preprocessing

The delay-and-sum imaging algorithm requires knowledge of the group velocity so that arrival times can be accurately calculated given a specific wave path. Since the waves are propagating in a plate, there is geometrical dispersion, and both the phase and group velocities are functions of frequency. It is assumed that a single mode is dominant, which for this work is the S_0 mode. To both minimize the effects of dispersion and reduce noise, all received signals are first filtered by time domain convolution with a Hanning-windowed tone burst. For
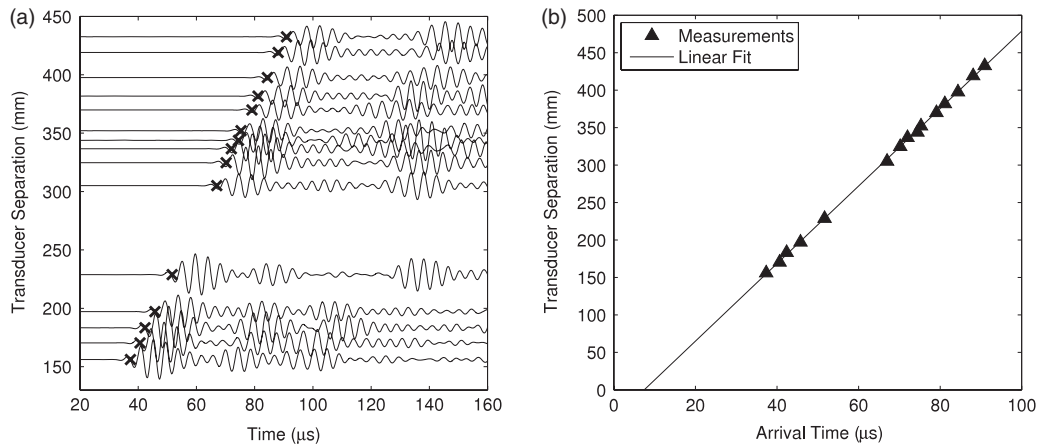
Figure 6. Group velocity calibration based upon a center frequency of 250 kHz. (a) Waterfall plot of direct signal arrivals versus transducer separation distance, and (b) transducer separation distance versus calculated arrival time of the direct signal.
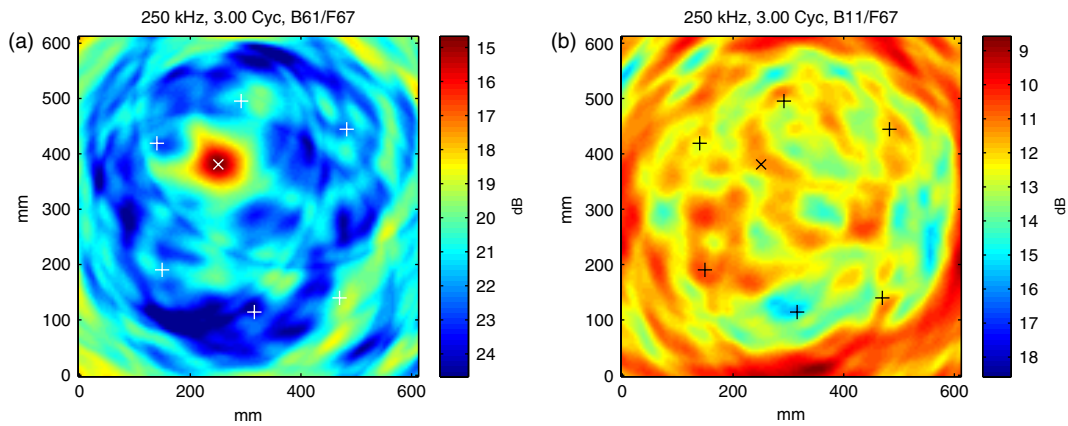
Figure 7. Typical images constructed from the data set recorded immediately after the 6 mm diameter hole was drilled. (a) Image constructed using the best baseline, which is well matched in temperature to the recorded data set, and (b) image constructed from a baseline with a temperature mismatch of about 2 °C. The + symbols are transducer locations and the × is the actual hole location.

the transducers and plate considered here, the practical range of frequencies which can be considered is approximately 150–300 MHz, which is below the A_1 cutoff frequency.

The second step is to calibrate the group velocity from the arrival times of the direct waves propagating between all transducer pairs. Arrival times are obtained from the envelope-detected signals by finding a threshold crossing point; the threshold is adaptively set to a percentage of the amplitude of the first arrival. Figure 6(a) illustrates the result of this process where all 15 signals are displayed in a waterfall plot; the transducer separation distance for each pair has determined the vertical spacing. Figure 6(b) is a plot of transducer separation distance versus arrival time. The slope of this curve is the group velocity, c_g, and the time axis intercept is a fixed time offset, t_{off}. Thus, the expected arrival time t_{arr} for a given propagation distance D is

$$t_{arr} = \frac{D}{c_g} + t_{off}. \qquad (6)$$

The third step is to scale each received signal based upon the amplitude of the first arrival. This scaling, which includes a correction for the reduction in amplitude with the square root of the distance, also serves to compensate for amplitude differences caused by transducer and bonding variations. If A_{ij} is the amplitude of the direct arrival from transducer pair ij, then the received signals are scaled as

$$\hat{w}_{ij}(t) = \frac{w_{ij}(t)}{A_{ij}} \sqrt{\frac{D_{ref}}{D_{ij}}}. \qquad (7)$$

In this equation $w_{ij}(t)$ is the filtered but unscaled signal, $\hat{w}_{ij}(t)$ is the filtered and scaled signal, D_{ij} is the distance between transducers i and j, and D_{ref} is a reference distance set equal to 1 m.

The final step is to calculate the envelope-detected differenced signals. Let $u_{ij}(t)$ be the difference between the current signal of interest, $\hat{w}_{ij}(t)$, and the baseline, $\hat{w}_{ij}^b(t)$, after filtering and scaling,

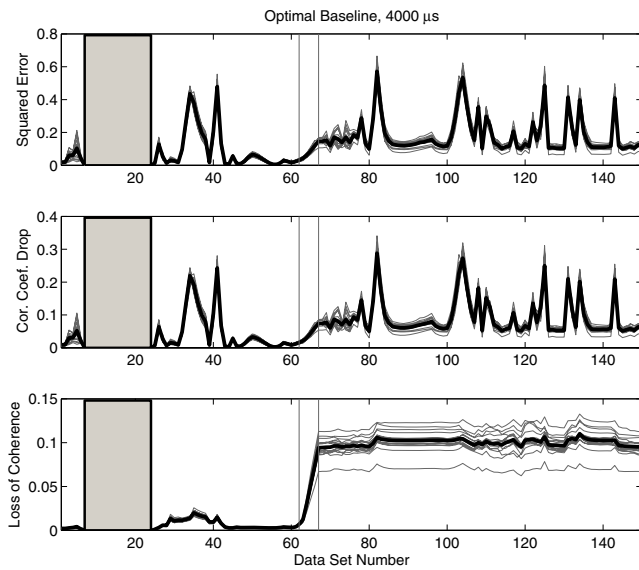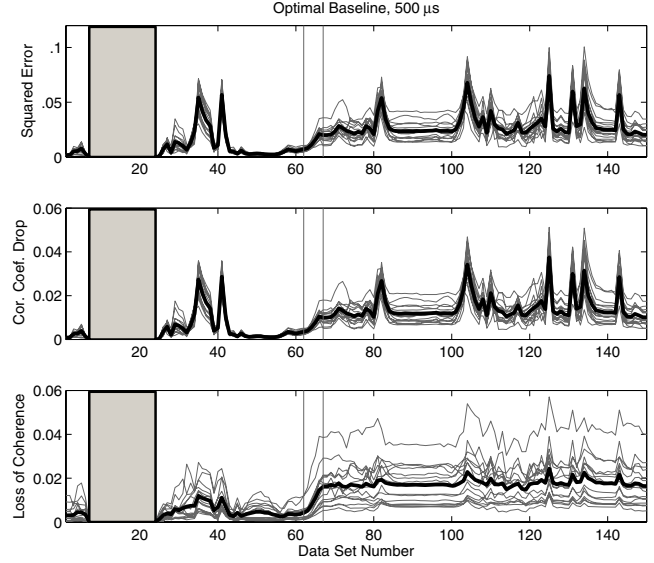$$u_{ij}(t) = \hat{w}_{ij}(t) - \hat{w}_{ij}^b(t). \qquad (8)$$
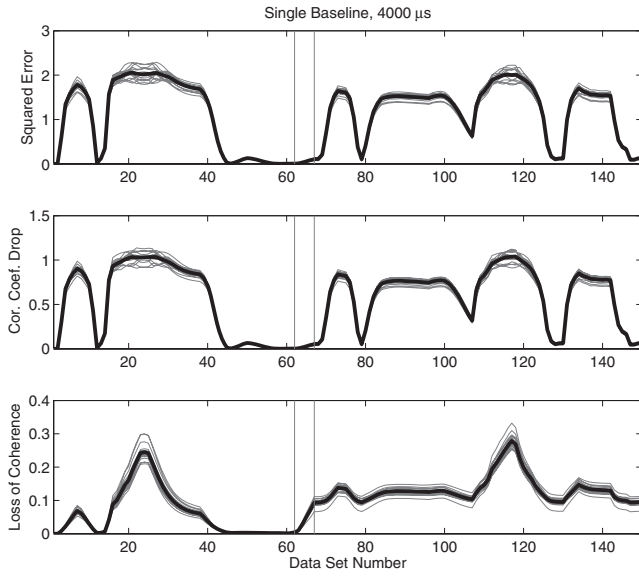
Figure 8. Detection results for the hole experiment using a single baseline and a 4000 μs time window: squared error (top), correlation coefficient drop (middle), and loss of coherence (bottom). The vertical lines bracket the data sets during which the hole was drilled and enlarged, the grey curves are the results for each transducer pair, and the heavy black curves are the average over all 15 transducer pairs.
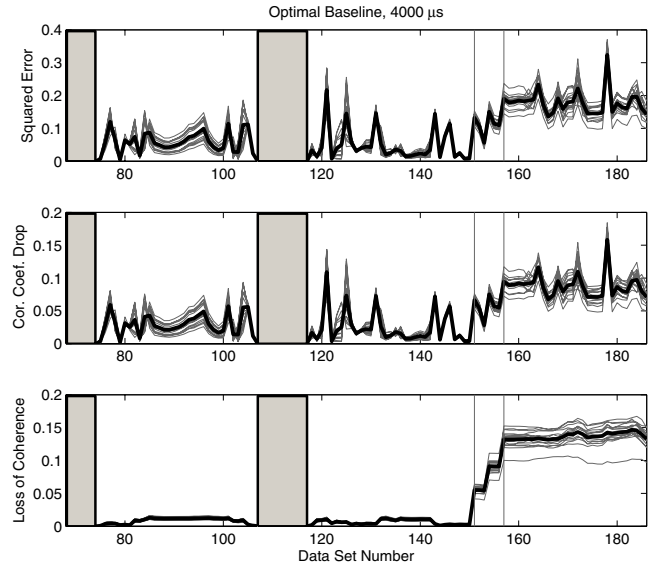
Figure 10. Detection results for the notch experiment using optimal baselines and a 4000 μs time window: squared error (top), correlation coefficient drop (middle), and loss of coherence (bottom). The shaded rectangles indicate the baseline data sets, the vertical lines bracket the data sets during which the notch was machined and enlarged, the grey curves are the results for each transducer pair, and the heavy black curves are the average over all 15 transducer pairs.

Figure 9. Detection results for the hole experiment using optimal baselines and a 4000 μs time window: squared error (top), correlation coefficient drop (middle), and loss of coherence (bottom). The shaded rectangles indicate the baseline data sets, the vertical lines bracket the data sets during which the hole was drilled and enlarged, the grey curves are the results for each transducer pair, and the heavy black curves are the average over all 15 transducer pairs.

Figure 11. Detection results for the hole experiment using optimal baselines and a 500 μs time window: squared error (top), correlation coefficient drop (middle), and loss of coherence (bottom). The shaded rectangles indicate the baseline data sets, the vertical lines bracket the data sets during which the hole was drilled and enlarged, the grey curves are the results for each transducer pair, and the heavy black curves are the average over all 15 transducer pairs.

The complex analytic signal is formed from this signal and its Hilbert transform, $v_{ij}(t)$,
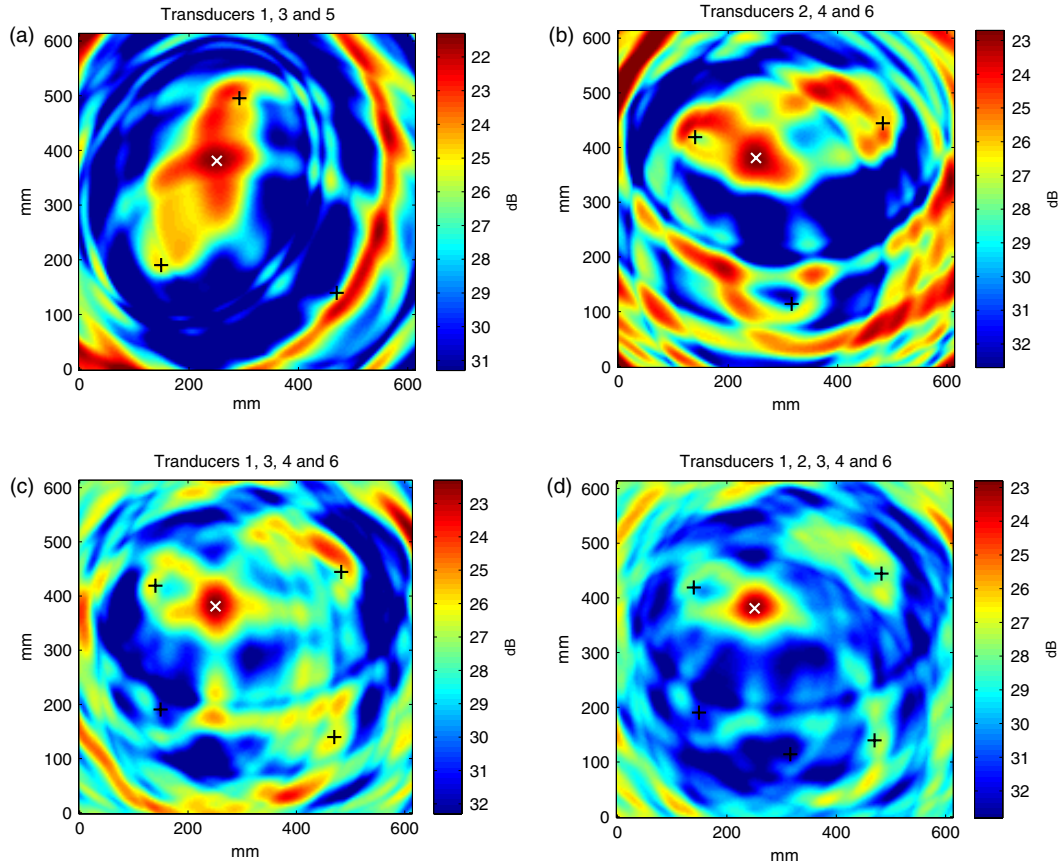
$$c_{ij}(t) = u_{ij}(t) + \mathrm{i}\, v_{ij}(t). \tag{9}$$

The envelope-detected residual, or differenced, signal, $r_{ij}(t)$,

is the magnitude of the analytic signal,

$$r_{ij}(t) = \sqrt{u_{ij}(t)^2 + v_{ij}(t)^2}. \tag{10}$$

The signals $r_{ij}(t)$ for the 15 transducer pairs are input to the imaging algorithm.

Figure 12. Images constructed after the 6 mm diameter hole was drilled using various numbers of transducers. The signal is data set 67 and the baseline is data set 61. (a) Transducers 1, 3 and 5, (b) transducers 2, 4 and 6, (c) transducers 1, 3, 4 and 6 and (d) transducers 1, 2, 3, 4 and 6. The + symbols are transducer locations and the × is the actual hole location.

4.2. Imaging algorithm

Changes in signals are imaged by a delay-and-sum algorithm [17]. At each point on the image at coordinates (x, y), the arrival time of a signal traveling from transmitting transducer i at (x_i, y_i) to the image point at (x, y) and on to receiving transducer j at (x_j, y_j) is computed as

$$t_{ij}(x, y) = t_{\text{off}}$$
$$+ \frac{\sqrt{(x_i - x)^2 + (y_i - y)^2} + \sqrt{(x_j - x)^2 + (y_j - y)^2}}{c_{\text{g}}}.$$
(11)

Each differenced signal is delayed by the calculated amount, and all signals are squared and averaged at each spatial location to obtain the image value, $E(x, y)$,

$$E(x, y) = \frac{1}{N_{\text{p}}} \sum_{i=1}^{N-1} \sum_{j=i+1}^{N} r_{ij}(t_{ij}(x, y)).$$
(12)

In this equation the number of transducer pairs is $N_{\text{p}} = N(N-1)/2$. For a single transducer pair, this imaging algorithm maps a single echo to an ellipse with the foci of the ellipse being the two transducer locations. As additional pairs are added, the ellipses intersect at defect locations and thus reinforce.

Two images are computed here to illustrate the algorithm using signals that were filtered by convolution with a

three-cycle, Hanning-windowed, 250 kHz tone burst. At this frequency, the group velocity c_{g} was computed to be 5.1524 mm μs^{-1} with an offset time t_{off} of 7.04 μs. Figure 7(a) shows an image obtained from data set #67, recorded shortly after the 6 mm diameter hole was drilled, using as baseline data set #61. This baseline signal is the one recorded immediately prior to drilling of the hole and thus is very well matched in temperature to signal #67. Figure 7(b) shows the corresponding image using data set #11 as the baseline, which has a temperature mismatch of about 2 °C. The scale for both images spans a 10 dB range, and each image is normalized to its peak value. The drilled hole is clearly imaged in figure 7(a) with a signal-to-noise ratio of about 4 dB, whereas there is little if any evidence of the hole in figure 7(b). Clearly a well-matched baseline is essential for localizing damage using this algorithm.

5. Results and discussion

5.1. Damage detection

Data were first analyzed by calculating the three differential features E_1, E_2 and E_3 using a fixed baseline and the entire recorded signal ($T = 4000 \,\mu$s). Results are shown for the hole experiment in figure 8, where the baseline was taken to be data set #1 and the three features are plotted versus data set number;
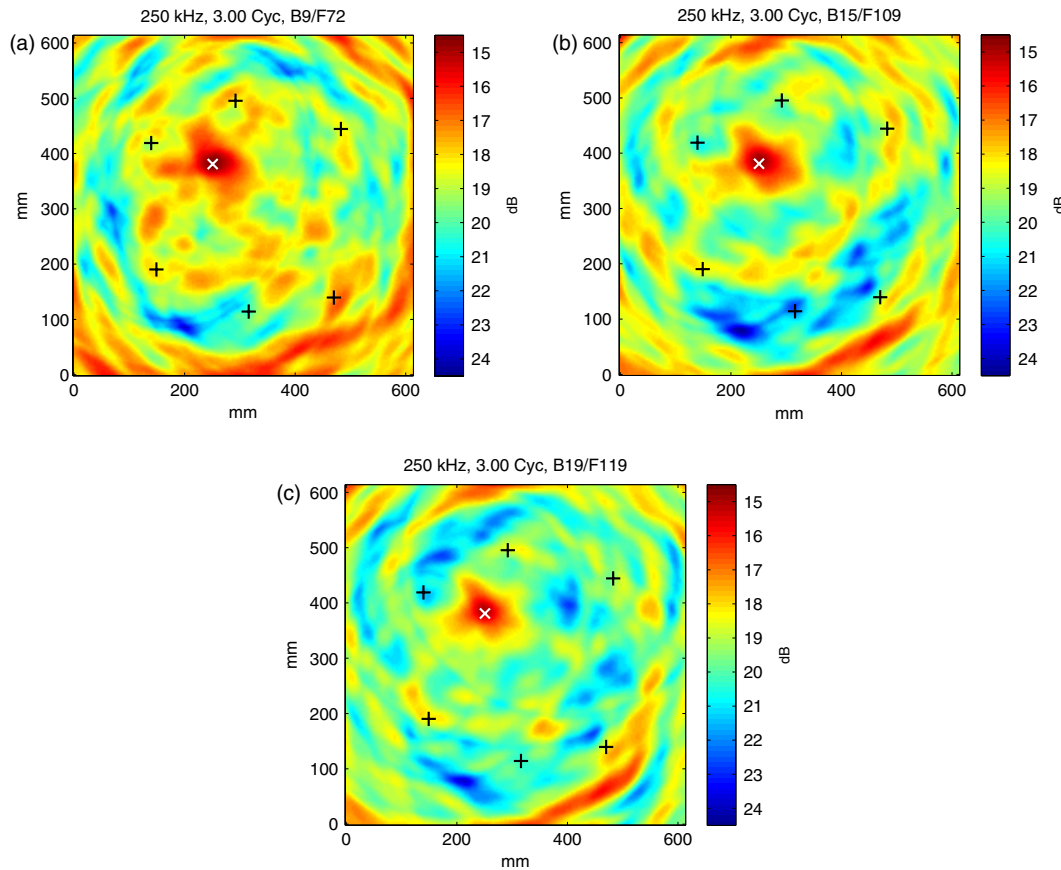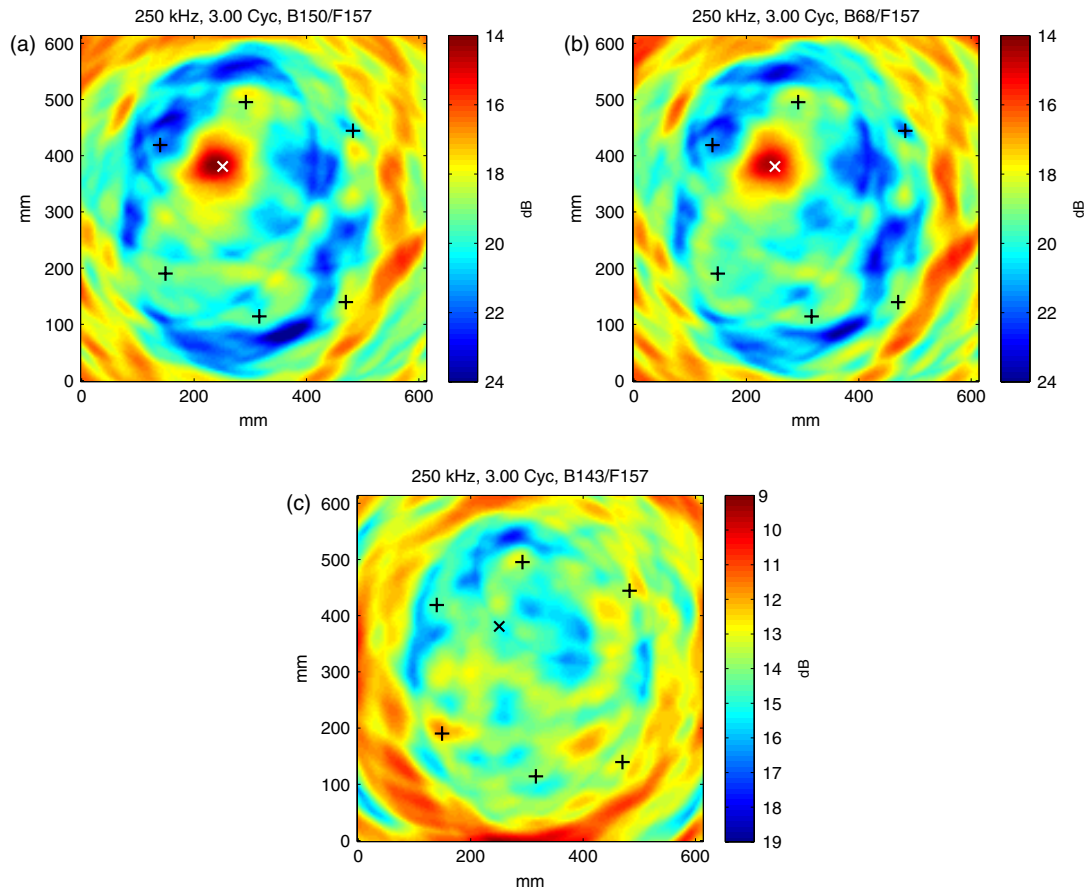
Figure 13. Images constructed from several data sets recorded after the 6 mm diameter hole was drilled using the optimal baselines. (a) Signals recorded about 1.5 h after the hole was drilled at a temperature of 19.1 °C, (b) signals recorded the next day at a temperature of 26.6 °C, and (c) signals recorded the next day at a temperature of 32.3 °C (bottom). The + symbols are transducer locations and the × is the actual hole location.

the heavy black curves are the average of each parameter over the 15 transducer pairs. The vertical lines bracket the data sets for which damage was introduced (#62–#67), so all signals to the left of the vertical lines should be categorized as 'no damage' and those to the right as 'damage.' For the normalized squared error E_1 and the correlation coefficient drop E_2, large values are strongly correlated to temperature changes rather than damage. In fact, increases caused by damage are barely detectable, being an order of magnitude smaller than changes resulting from temperature variations. It is interesting to note that the performance of E_1 and E_2 is essentially the same but with a ×2 scale factor difference between them. This relationship is what would be predicted by a phase shift between two sinusoidal signals with no amplitude change. The loss of local coherence performs somewhat better, with damage causing both a clearly defined jump and a permanent elevation of the minimum value. However, changes in E_3 resulting from temperature variations are of the same order of magnitude as the increase caused by damage, and it is thus not possible to set a fixed detection threshold. Results for the notch experiment, although not shown, are similar.

Data were next analyzed by selecting the baseline as per the optimal baseline selection procedure of section 3.3. For the hole experiment, the baselines were data sets #7 through #24, and for the notch experiment they were data sets #68 through #74 and #107 through #117; these baselines span the temperature range of interest for both cases and are indicated by the shaded rectangles in the upcoming figures. The three differential features were calculated using the optimal baseline and the entire signal length of 4000 μs. Results are plotted in figures 9 and 10 for the hole and notch, respectively. The temperature spacing of the baseline data sets was not completely uniform, varying from 0.5 to 3 °C, which resulted in temperature differences between the signal and the best baseline ranging from zero to as much as 1.5 °C. The squared error and correlation coefficient drop are still unable to detect the damage in the presence of even these small temperature changes. However, the loss of local coherence is able to detect the larger hole sizes (4 mm diameter and above) and all of the notch increments with no false alarms by using a damage detection threshold of 0.04. It can also be seen by the loss of coherence results in both figures 9 and 10 that only one sensor pair is necessary for the detection of damage; however, additional pairs provide redundancy and can reduce the number of false alarms.

The importance of using the long time signal regime is illustrated by detection results computed from a smaller time window. Instead of the 4000 μs window, which corresponds to a travel distance of about 20 m for the S_0 mode, the optimal baseline and the differential features were determined from

Figure 14. Images constructed from the data set recorded immediately after the notch was enlarged to its final size. (a) Baseline recorded immediately prior to initiation of the notch, (b) baseline recorded two days prior to initiation of the notch but at a well-matched temperature, and (c) baseline recorded under ambient conditions about 3 h prior to initiation of the notch but with a temperature mismatch of about 1.5 °C. The + symbols are transducer locations and the × is the actual hole location.

a window of 500 μs. This smaller window corresponds to a travel distance of about 2.5 m, which includes some edge reflections but is not so long for the signal to be considered diffuse-like. Results for the hole are shown in figure 11, and comparison to the 4000 μs window results of figure 9 indicates a marked degradation in detection performance. The reason for the improved performance of the longer window is that the plate boundaries generate multiple reflections which repeatedly travel through the region of damage. Thus, the later time portions of the received signal are more likely to deviate from the baseline by a greater amount than the earlier time portions, resulting in a greater detection sensitivity for a longer time window. This effect will most likely not be as pronounced for a real aerospace structure with lossy boundaries, but suggests that signals should be recorded for a long enough time window to capture most of the reverberating energy.

5.2. Damage localization

The delay-and-sum imaging method described in section 4 was used to create multiple images of both the hole and the notch using various combinations of signal and baseline data sets. Prior to imaging, all signals were digitally filtered by convolution with a three-cycle, Hanning-windowed tone burst centered at 250 kHz.

Figure 12 illustrates the effect of the number of transducers on the imaging quality for the same image of figure 7(a). Shown are images from two different combinations of three transducers, the four corner transducers, and one combination of five transducers. All images are normalized to the amplitude of the flaw response, and it can be seen that the image quality improves as more transducers are added. All transducer combinations shown here are able to localize the damage within the bounding polygon formed by the transducers, but image artifacts outside of the bounding polygon decrease as the number of transducers increases. All six transducers are used for the images shown in the rest of this paper.

Figure 13 shows three images of damage after the 6 mm diameter hole was drilled but with data sets recorded at three different temperatures. The baselines used for the imaging process are those determined via the optimal baseline selection process described in section 3.3. Figure 13(a) shows the image constructed from data set #72, which was recorded about 1.5 h after the hole was drilled and after the plate was cooled to a nominal temperature of 19.1 °C. Figures 13(b) and (c) are constructed from data sets #109 and #119, recorded the next day and at nominal temperatures of 26.5 °C and 32.3 °C, respectively. The optimal baselines for the three figures are
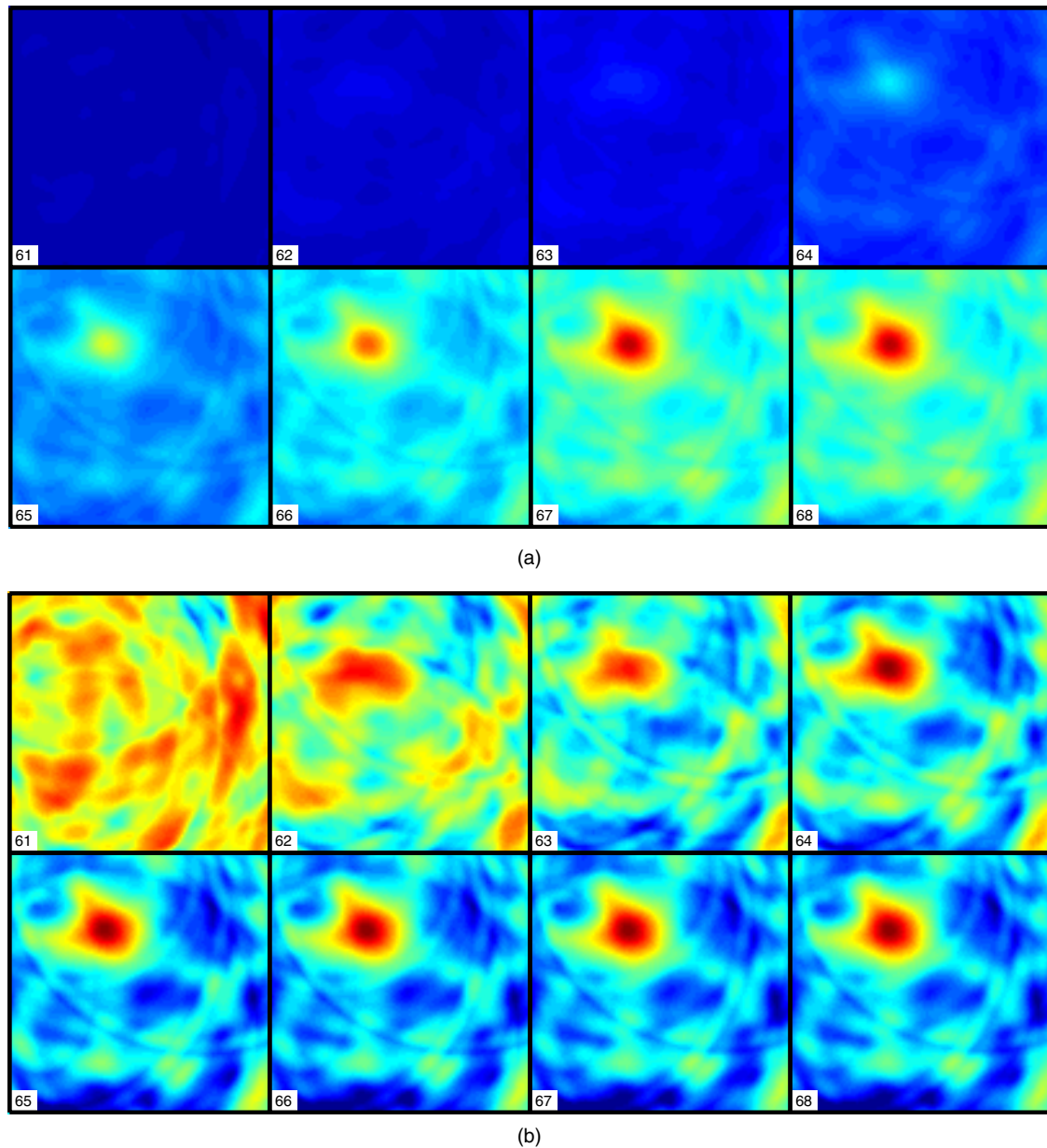
Figure 15. Progression of images (400 × 400 mm region in the center of the plate) as the hole is enlarged from 1.5 mm diameter (data set #62) to its final diameter of 6 mm (data set #67). (a) Linear scale and (b) 10 dB scale normalized to the peak amplitude of each image.

data sets #9, #15 and #19, respectively. Despite the fact that the data sets for the three images were recorded at different times and temperatures, the images are very similar and effectively localize the drilled hole. Not unexpectedly, the image quality is not as good as that of figure 7(a), where the baseline was recorded immediately before the hole was drilled and the data set of interest was recorded immediately after, yielding the best possible temperature match.

The three images of figure 13, although effectively localizing the simulated damage, contain significant artifacts away from the damage location. There are three primary sources of these artifacts. The first is caused by imaging with only a small number of transducer pairs. The first scattered arrival recorded from each pair contributes an ellipse to the image, and these ellipses all pass through the point

of damage and reinforce. However, there are still vestiges of these ellipses away from the damage location which contribute to the background noise; these artifacts are more pronounced in the images of figure 12 created from fewer transducers. The second source of imaging artifacts is multiple scattering between the damage and the structural boundaries. These multiply scattered signals are not removed by baseline subtraction and thus contribute to imaging artifacts. The third source of artifacts is caused by imperfect baseline subtraction arising from temperature mismatch. These artifacts can vary from being insignificant to completely obscuring the damage as the temperature mismatch increases.

Figure 14 shows three images from the notch experiment that illustrate the degradation in image quality caused by temperature mismatch. All three of the images are based

(a)

(b)
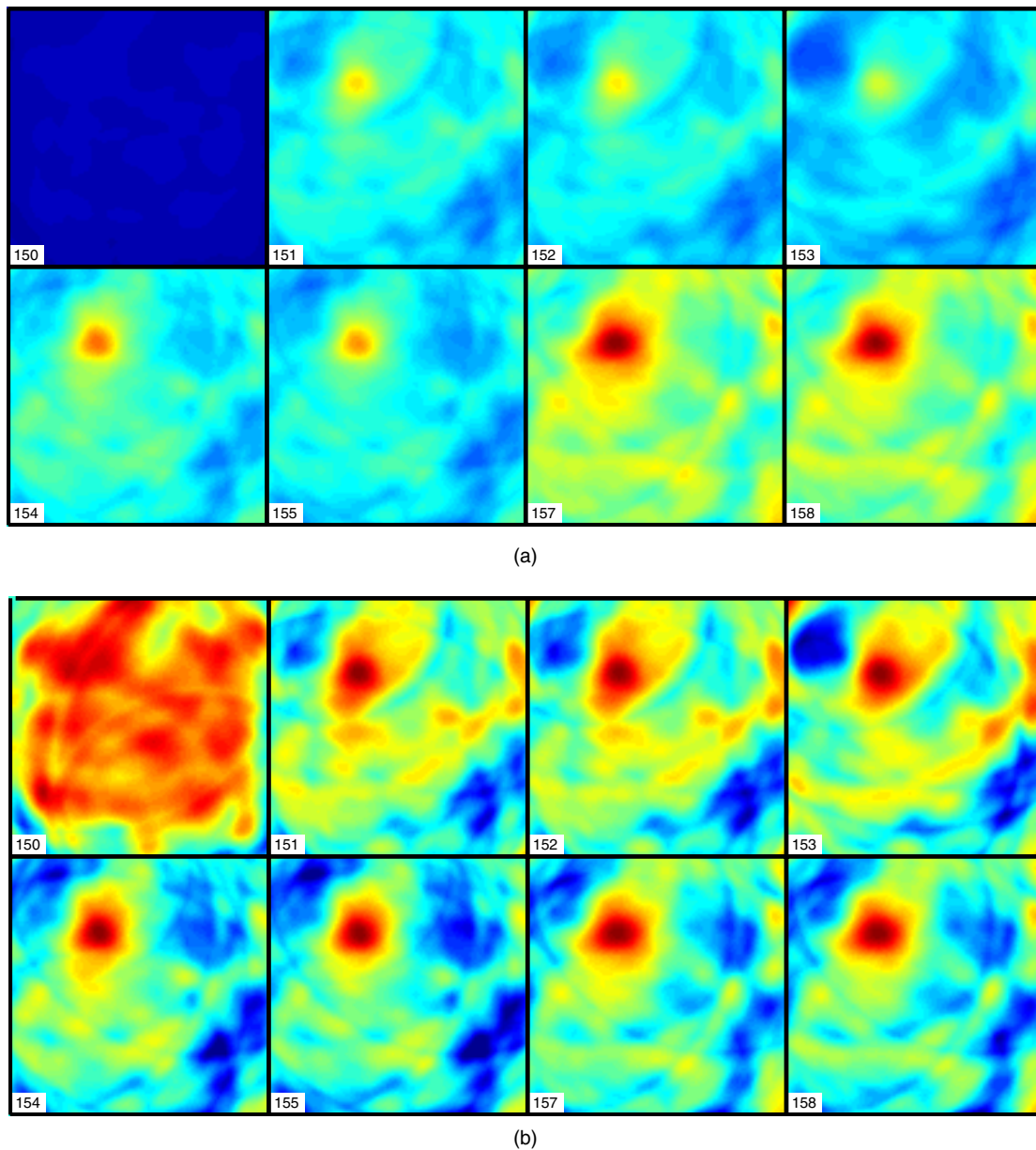
Figure 16. Progression of images (400 × 400 mm region in the center of the plate) as the notch is enlarged from a length of 3.2 mm (data set #151) to 6.4 mm (data set #154) to its final length of 9.5 mm (data set #157). (a) Linear scale, and (b) 10 dB scale normalized to the peak amplitude of each image.

upon data set #157, recorded immediately after the notch was enlarged to its final size. The baseline for figure 14(a) is data set #151, which was recorded immediately before the notch was initiated; it is thus most likely to be the best possible match since it was recorded at nominally the same temperature as data set #157 and with the smallest possible separation in time. The temperature difference between these two data sets was measured to be about 0.2 °C. Note that the center of the localized region of damage is slightly to the left of the hole center, which is consistent with the actual notch location. The baseline for figure 14(b) is data set #68, which is the optimal baseline. This data set was recorded two days prior to initiation of the notch, and the measured temperature difference is about 0.3 °C. For figure 14(c), data set #143 is used as the

baseline. This data set was recorded under ambient laboratory conditions about three hours before the notch was initiated. The temperature was not recorded, but was ultrasonically measured to be about 1.5 °C higher than that of data set #157. As expected, the best image, figure 14(a), is based upon using the baseline data set recorded just prior to the initiation of damage, but the image of figure 14(b) using a much earlier data set is also quite good. As seen in figure 14(c), all evidence of damage localization is completely obscured as a result of using a baseline set with a temperature mismatch of about 1.5 °C, which is consistent with the result from the hole experiment shown in figure 7(b), where there was a mismatch of 2 °C.

It is possible to evaluate the potential of this imaging method for sizing defects by examining a series of images

13
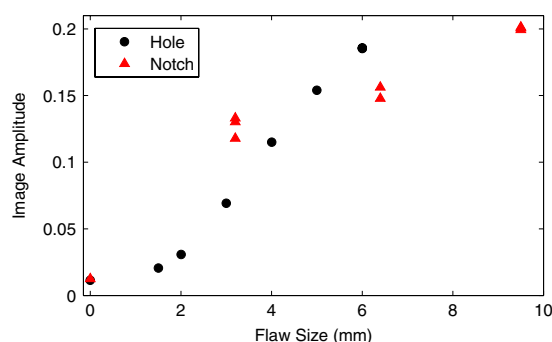
Figure 17. Image amplitude at the damage location versus flaw size (diameter or length) for the hole and notch data.

as both the hole and the notch are introduced and enlarged to their final sizes. Figure 15(a) shows a series of images of the hole displayed using a common linear scale. The eight images correspond to hole diameters of 0, 1.5, 2, 3, 4, 5, 6 and 6 mm, and it is clear that the amplitude of the image at the hole location is strongly correlated to the hole size. The degree of localization as a function of hole size can best be seen on a logarithmic scale, and the same images are shown in figure 15(b) on a 10 dB scale with each image separately normalized by its peak value. It can be seen that once the flaw is unambiguously detected, at a diameter of about 3 mm, the degree of localization is not strongly correlated to the flaw size. Similar results are obtained from the notch data, which are shown in figure 16. The images suggest that amplitude rather than image extent is best correlated to flaw size. Figure 17 clearly shows the monotonic relationship between image peak amplitude and flaw size for both the hole and the notch.

6. Summary and conclusions

A two-stage strategy for detection and subsequent localization and characterization of damage in a bounded aluminum plate has been demonstrated for artificial defects in the presence of temperature variations. Critical to the success of this strategy is the effective use of the long time diffuse-like regime of the recorded signals for damage detection. When comparing such a signal to a baseline, the slope of the time shift versus transit time curve can be determined from the short time cross correlation and then related to the temperature difference, enabling temperature monitoring from the ultrasonic signals without additional sensors. If a set of baselines is recorded which span the temperature range of interest, then the optimal baseline can be selected which best matches the current signal being analyzed. For the data shown here, achieving a match within about $\pm 2\,°C$ is sufficient for the detection of damage based upon a differential feature quantifying the loss of local temporal coherence.

The same optimal baseline can then be used to calculate residual (differential) signals which are used for imaging the location of the damage. A delay-and-sum algorithm, which maps echoes in the residual signals to ellipses, was shown to be effective for damage localization. For the experimental data considered here, a temperature match of $\pm 0.5\,°C$ or better was

required for effective localization. It was further shown that image amplitude rather than spatial extent correlates best to flaw size.

These results are significant because they demonstrate effective damage detection, localization and characterization as applied to both complex signals and changing environmental conditions. The importance of temperature matching for both detection and localization is clearly evident. Even though the plate itself is simple geometrically, it is complex from a wave propagation standpoint because of the strong multiple reflections and multiple Lamb wave modes, and is thus an effective test bed for initial algorithm development.

Acknowledgment

References

[1] Giurgiutiu V, Bao J and Zhao W 2003 Piezoelectric wafer active sensor embedded ultrasonics in beams and plates *Exp. Mech.* **43** 428–49
[2] Rose J L 2000 Guided wave nuances for ultrasonic nondestructive evaluation *IEEE Trans. Ultrason. Ferroelectr. Freq. Control* **47** 575–83
[3] Cawley P and Simonetti F 2005 Structural health monitoring using guided waves—potential and challenges *Proc. 5th Int. Conf. on Struct. Health Monitoring* ed F-K Chang (Lancaster, PA: DEStech Publications, Inc.) pp 503–10
[4] Michaels T E and Michaels J E 2004 Sparse ultrasonic transducer array for structural health monitoring *Review of Progress in Quantitative Nondestructive Evaluation* vol 23B ed D O Thompson and D E Chimenti (New York: American Institute of Physics) pp 1468–75
[5] Gao H, Shi Y and Rose J L 2005 Guided wave tomography on an aircraft wing with leave in place sensors *Review of Progress in Quantitative Nondestructive Evaluation* vol 24B ed D O Thompson and D E Chimenti (New York: American Institute of Physics) pp 1788–94
[6] Mal A, Ricci F, Banerjee S and Shih F 2005 A conceptual structural health monitoring system based on vibration and wave propagation *Struct. Health Monitoring* **4** 283–93
[7] Mal A K, Banerjee S, Monaco E and Lecce L 2006 Autonomous health monitoring of a stiffened composite plate *Proc. SPIE Conf. on Health Monitoring and Smart Nondestructive Evaluation of Structural and Biological Systems V*; *Proc. SPIE* **6177** 617701
[8] Michaels J E, Lu Y and Michaels T E 2004 A comparison of feature-based classifiers for ultrasonic structural health monitoring *Proc. SPIE Conf. on Health Monitoring and Smart Nondestructive Evaluation of Structural and Biological Systems IV*; *Proc. SPIE* **5394** 363–74
[9] Lu Y and Michaels J E 2007 Consideration of surface variations on ultrasonic structural health monitoring *Proc. 6th Int. Conf. on Structural Health Monitoring* ed F-K Chang (Lancaster, PA: DEStech Publications, Inc.) pp 1275–82
[10] Lemistre M and Balageas D 2001 Structural health monitoring system based on diffracted Lamb wave analysis by multiresolution processing *Smart Mater. Struct.* **10** 504–11
[11] Tua P S, Quek S T and Wang W 2004 Detection of cracks in plates using piezo-actuated Lamb waves *Smart Mater. Struct.* **13** 643–60

[12] Michaels T E, Michaels J E, Mi B and Ruzzene M 2005 Damage detection in plate structures using sparse transducer arrays and acoustic wavefield imaging *Review of Progress in Quantitative Nondestructive Evaluation* vol 24A, ed D O Thompson and D E Chimenti (New York: American Institute of Physics) pp 938–45

[13] Zhao X, Gao H, Zhang G, Ayhan B, Yan F, Kwan C and Rose J 2007 Active health monitoring of an aircraft wing with embedded piezoelectric sensor/actuator network: I. Defect detection, localization and growth monitoring *Smart Mater. Struct.* **16** 1208–17

[14] Wang C H, Rose J T and Chang F-K 2004 A synthetic time-reversal imaging method for structural health monitoring *Smart Mater. Struct.* **13** 415–23

[15] Michaels J E and Michaels T E 2006 Enhanced differential methods for guided wave phased array imaging using spatially distributed piezoelectric transducers *Review of Progress in Quantitative Nondestructive Evaluation* vol 25B, ed D O Thompson and D E Chimenti (New York: American Institute of Physics) pp 837–44

[16] Michaels J E and Michaels T E 2007 An integrated strategy for detection and imaging of damage using a spatially distributed array of piezoelectric sensors *Proc. SPIE Conf. on Health Monitoring of Structural and Biological Systems*; *Proc. SPIE* **6532** 653203

[17] Michaels J E and Michaels T E 2007 Guided wave signal processing and image fusion for in situ damage localization in plates *Wave Motion* **44** 482–92

[18] Fromme P 2007 Monitoring of plate structures using guided ultrasonic waves *Review of Progress in Quantitative Nondestructive Evaluation* vol 27, ed D O Thompson and D E Chimenti (New York: American Institute of Physics)

[19] Michaels J E and Michaels T E 2005 Detection of structural damage from the local temporal coherence of diffuse ultrasonic signals *IEEE Trans. Ultrason. Ferroelectr. Freq. Control* **52** 1769–82

[20] Liu D, Kang G, Li L, Chen Y, Vasudevan S, Joines W, Liu Q H, Krolik J and Carin L 2005 Electromagnetic time-reversal imaging of a target in a cluttered environment *IEEE Trans. Antennas Propag.* **53** 3058–66

[21] Konstantinidis G, Drinkwater B W and Wilcox P D 2006 The temperature stability of guided wave structural health monitoring systems *Smart Mater. Struct.* **15** 967–76

[22] Mazzeranghi A and Vangi D 1999 Methodology for minimizing effects of temperature in monitoring with the acousto-ultrasonic technique *Exp. Mech.* **39** 86–91

[23] Olson S E, DeSimio M P and Derriso M M 2005 Structural health monitoring incorporating temperature compensation *Proc. 5th Int. Conf. on Structural Health Monitoring* ed F-K Chang (Lancaster, PA: DEStech Publications, Inc.) pp 1653–42

[24] Lu Y and Michaels Jennifer E 2005 A methodology for structural health monitoring with diffuse ultrasonic waves in the presence of temperature variations *Ultrasonics* **43** 717–31

[25] Weaver R L and Lobkis O I 2000 Temperature dependence of diffuse field phase *Ultrasonics* **38** 491–4